

Article

The Hot Tensile Properties, Fracture Features, and Microstructure Evolution of As-Cast 7005 Aluminum Alloy

Erli Xia ^{1,2} , Tuo Ye ^{1,2}, Limei Liu ^{1,2}, Wei Liu ^{1,2}, Huanyu Yue ², Jian Tang ² and Yuanzhi Wu ^{1,2,*}

¹ Research Institute of Automobile Parts Technology, Hunan Institute of Technology, Hengyang 421002, China; 2021001046@hnit.edu.cn (E.X.)

² School of Intelligent Manufacturing and Mechanical Engineering, Hunan Institute of Technology, Hengyang 421002, China

* Correspondence: 2013001767@hnit.edu.cn

Abstract: In order to explore the hot deformation behaviors of the as-cast 7005 aluminum alloy, a number of hot tensile tests with four temperatures (100, 200, 300, and 400 °C) and three strain rates (0.001, 0.01, and 0.1 s⁻¹) were performed. The Johnson–Cook model was used to express the relationship between stress, strain, strain rate, and temperature. Scanning electron microscopy (SEM), optical microscopy (OM), and transmission electron microscopy (TEM) were selected to reveal fracture features and microstructure evolution of the studied alloy. The results indicate that the flow stress level of the alloy reduces with increases in the deformation temperature and decreases in the strain rate. The established Johnson–Cook model can be employed to characterize the thermal flow behavior of the experimental alloy. The grains near the fracture surface were elongated, and a certain number of holes were found after deformation at 400 °C. The alloy exhibits obvious ductile fracture features. The dimple is deep with high quantity. Due to the plastic deformation, a high-density dislocation structure is found in the material. High-temperature conditions promote the annihilation of dislocation, and, as a result, the dislocation density decreases gradually with the increase in temperature. In addition, a certain number of precipitates were found in the alloy after high-temperature tension.

Keywords: 7005 aluminum alloy; hot tensile behavior; the Johnson–Cook model; microstructure evolution; fracture features



Citation: Xia, E.; Ye, T.; Liu, L.; Liu, W.; Yue, H.; Tang, J.; Wu, Y. The Hot Tensile Properties, Fracture Features, and Microstructure Evolution of As-Cast 7005 Aluminum Alloy. *Metals* **2024**, *14*, 125. <https://doi.org/10.3390/met14010125>

Academic Editor: Thomas Niendorf

Received: 27 December 2023

Revised: 15 January 2024

Accepted: 17 January 2024

Published: 20 January 2024



Copyright: © 2024 by the authors. Licensee MDPI, Basel, Switzerland. This article is an open access article distributed under the terms and conditions of the Creative Commons Attribution (CC BY) license (<https://creativecommons.org/licenses/by/4.0/>).

1. Introduction

With the growing seriousness of environmental pollution and energy shortage problems, lightweight structural designs play an increasingly important role in the automobile, navigation, aerospace, and other industries [1–3]. In the automobile field, energy saving and emission reduction are challenging problems [4]. In the navigation field, corrosion resistance is one of the concerning factors [5]. In the aerospace field, excellent strength and lightness are crucial considerations [6]. Apart from the properties mentioned above, industries across the board require stable and sustained performance, and simple and highly effective forming [7,8]. Structural optimization is one of the feasible methods for solving those problems [9]. In addition, the development of low-density and high-strength materials is the most effective approach to realizing lightweight design, leading to enhanced performance, and outstanding forming ability [10,11].

During the process of materials development and practical application, different kinds of aluminum alloys have been fabricated. Adding Zn, Mg, Cu, and other elements into the aluminum element can produce 7xxx series aluminum alloys, which have a high strength-to-weight ratio and excellent toughness characteristics [12,13]. This series of aluminum alloys has superior mechanical properties with outstanding processing and formability performance. However, in the process of manufacturing and actual application, these aluminum alloy components will withstand various complex working conditions, such as

carrying complex tensile loads with high temperatures. Therefore, it is of great significance to investigate the hot tensile mechanical behavior of 7xxx series aluminum alloys at high temperatures [14–16]. The 7xxx series aluminum alloys are heat-treatable, and their precipitation sequence is generally believed to be SSSS \rightarrow GP Zones \rightarrow η' \rightarrow η [17]. Compared to commercial alloys such as 7075 and 7050 with high Zn, Mg, and Cu contents, the 7005 alloy has relatively low Mg, Zn, and Cu contents [18]. Therefore, it has excellent plastic formability and welding performance, and it can be extruded into thin-walled hollow profiles with various complex sections [19], which are commonly used as structural materials for components such as frames and crossbars, and civil engineering structures, such as bridges [20]. However, with the development of modern aerospace and transportation industries, the performance of this alloy needs to be further improved.

Abundant studies have shown that the mechanical behavior of alloys at high temperatures is significantly different from that at room temperature. Chen et al. [21] investigated the compression mechanical properties of extruded 7005 aluminum alloy at temperatures ranging from 350 to 550 °C. The flow stress increases with the increase in strain rate and decreases with the increase in deformation temperature. Their research confirmed that the microstructure of the material plays a decisive role in the mechanical properties of the material. Duan et al. [22] studied the effects of different equal-diameter angular extrusion parameters and annealing processes on the tensile mechanical properties of the 7005 alloy. The results showed that both extrusion parameters and heat treatment processes would affect the size of the grain structure of the material, thus affecting the comprehensive properties of the material. Jiang et al. [23] studied the microstructure and mechanical properties of thixoforming 7005 aluminum alloy. Microstructure evolution results showed that the thixoforming parameters and heat treatment process have significant effects on the grain structure of the material, thus regulating its mechanical properties. Reference [24] has reported that the fracture mechanism of AA7075 is altered from a ductile fracture in lower tensile temperatures to a brittle fracture under high tensile temperatures. In addition, as the temperature increases, the elongation first increases and then decreases. The hot deformation behaviors of 7075 aluminum alloys manufactured by laser-directed energy deposition were investigated by Fu et al. [25]. Their research outcomes indicated that, for as-printed samples, the strengthening mechanism derived from dislocation strengthening and Orowan strengthening, while for heat-treated samples, Orowan strengthening played a leading role. In summary, with the continuous development of materials, their application range will be more and more extensive. As a consequence, the microstructure of materials will also undergo different evolution in complex service environments, resulting in different responses in the mechanical properties of materials. Therefore, the study of the mechanical properties and microstructural evolution mechanisms of materials under different deformation conditions is the foundation for expanding the application range of materials.

During the service of aluminum alloy components, they may be exposed to higher temperature environments, during which the mechanical properties of the alloy may undergo certain changes and have an impact on the overall reliability of the components. Meanwhile, the hot forming parameters, such as temperature and strain rate, are decisive to the processing accuracy and quality of the products. However, considering the previous research, there has been a lack of studies on the hot tensile behavior and deformation mechanism of the 7005 alloy. Based on the above research background, this study selected the as-cast 7005 alloy as the research object. By adopting hot tensile experiments, the influence of temperature and strain rate on the response of the tensile mechanical properties was analyzed. With the assistance of OM, SEM, and TEM, fracture features and microstructure evolution mechanisms were analyzed. The main alloying elements in the 7005 alloy are Zn, Mg, and Cu, and their forming process, heat treatment process, deformation mechanism, and microstructure evolution are comparable to the 7xxx series aluminum alloys. The research results for the 7005 aluminum alloy may provide some guidance for the performance

improvement of 7xxx series aluminum alloys, and facilitate industrial material selection for structural components.

2. Description of Material and Experiment Methods

The experimental 7005 alloy ingot was manufactured by the semi-continuous casting method, and its chemical components are shown in Table 1.

Table 1. The chemical composition of the studied 7005 alloy.

Composition	Zn	Mg	Si	Mn	Fe	Cu	Al
Content (wt %)	4.5	1.3	0.25	0.25	0.15	0.05	Bal.

The tensile sample was prepared by wire-cutting processing, and the dimensions of the test sample are displayed in Figure 1. Before the test, the sample was heated to a target temperature with a heating rate of 5 °C/s. For each tensile condition, three repetitive tensile tests were performed to guarantee the reliability of the experimental data. In order to eliminate the temperature gradient in the interior of the material, the sample was held for another 5 min. A Gleeble3500 machine (DSI, St. Paul, MN, USA) was equipped with a computer, by which the stress and strain data can be recorded.

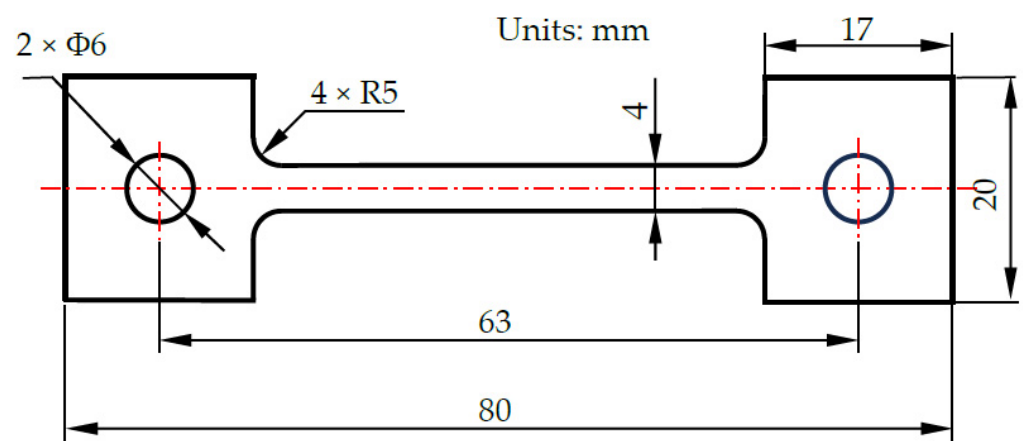


Figure 1. Dimensions of the high-temperature tensile specimen of the as-cast 7005 alloy.

After the high-temperature tensile test, the fracture morphology of the tensile specimen was observed using a scanning electron microscope (FEI, Hillsboro, OR, USA). The wire-cutting machine was used to cut the fracture specimen for preparing the OM sample, as illustrated in Figure 2. After grinding and polishing, the OM sample was corroded in 5% HBF₄ solution for 1–3 min with 20 V voltage. The microstructure of the sample was observed using an optical microscope (AX10, Zeiss, Oberkochen, Baden-Württemberg, Germany). In order to prepare the TEM sample, a thin plate was obtained from the fracture samples. A rounded sample with a 3 mm diameter was processed by punching the sliced plate. The sample was then mechanically ground to about 0.08 mm thickness. In order to create a uniform thin area in the sample, it needed further thinning via twin-jet electro-polishing in a methanol and nitric acid mixed solution with a volume ratio of 7:3, a temperature of −30~−20 °C, and a voltage of 20 V. The microstructures were observed using a TEM Talos F200X (FEI, Hillsboro, OR, USA) with 200 kV voltage. Based on the above introduction, it should be mentioned that the result of the micro examination only shows a very small part of the sample.

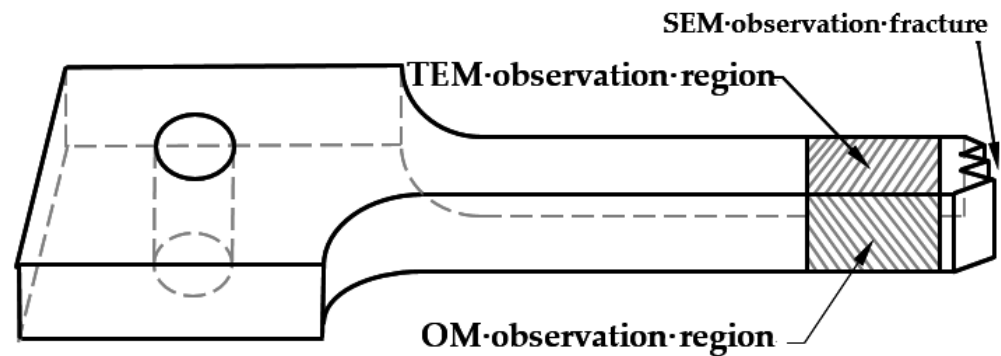


Figure 2. The observation region of the sample.

3. Results and Discussion

3.1. The True Stress–Strain Curves

The true stress–true strain curves of the as-cast 7005 alloy under different temperatures and strain rates are illustrated in Figure 3. In fact, the high-temperature tensile curve is the result of a combined effect of strengthening, softening, and damage effects. Initially, the flow stress increases rapidly with the increase in strain. In the initial stage of deformation, the dislocation density inside the material increases. Due to the small deformation and short deformation time, the dynamic recovery and recrystallization are not significant [26]. A pileup of dislocations occurs, and the deformation resistance of the material is improved. The strain-hardening effect is dominant. Thus, the flow stress increases rapidly. With the increase in strain, the flow stress increases gently. During this stage, the energy stored in the alloy increases, and softening behaviors such as dynamic recovery and recrystallization occur, which partially counteracts the effect of work hardening. As a consequence, the flow stress tends to be gentle [27–29]. A further increase in the strain leads to the alloy sample entering the failure fracture stage. The micropores in the material nucleate and grow, and the adjacent pores polymerize, which eventually leads to the fracture of the tensile specimen.

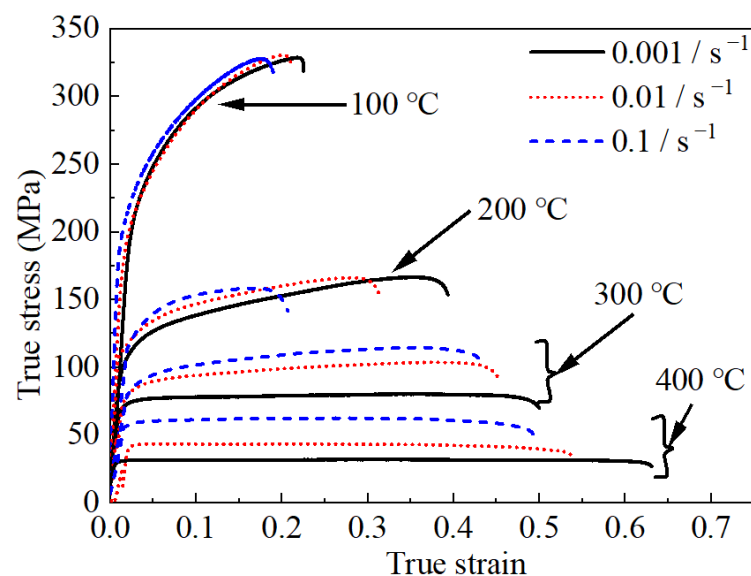


Figure 3. The true stress–strain curves of the as-cast 7005 alloy at different tensile parameters.

It can be seen from Figure 3 that when the tensile temperature is 100 °C, the flow stress of the 7005 alloy is not sensitive to the strain rate. In this deformation condition, the yield stress touches 180 MPa and the true strain of the alloy is between 0.2 and 0.25. Due to the low deformation temperature, the thermal motion of the atoms is not obvious, the

binding force between atoms is strong, and the deformation resistance remains at a high level. Therefore, the maximum elongation of the alloy is limited, and the alloy exhibits a relatively high strength. When the tensile temperature increases to 200 °C, the difference in the elastic deformation stage under the conditions of different strain rates is not obvious, and the yield stresses are around 118 MPa. In the plastic deformation stage, the flow stress increases gradually with the increase in strain rate. In addition, the maximum elongation of the material increased significantly compared with that in 100 °C tensile deformation. Since the high temperature can facilitate the motion of the atom, the binding force between atoms becomes weaker, the resistance to dislocation movement decreases, and grain boundary sliding is more likely to occur. The characteristics of flow stress with the tensile temperature increased to 300 °C are shown in Figure 3. It can be observed that the yield and tensile strength of the material increase significantly with the increase in strain rate. However, the strength is significantly lower than that at 200 °C, and the maximum elongation is increased to 0.45. As the temperature continues to climb, the atoms become more mobile, leading to pronounced dynamic recovery, which results in a decrease in strength and an increase in maximum elongation. The flow stress at the tensile temperature of 400 °C is displayed in Figure 3. The yield stress is lower than 60 MPa, and the strain-hardening effects are not obvious in the plastic deformation stage. Because the high-temperature softening process significantly weakens the strain strengthening of the material, dynamic recrystallization begins to occur, and some of the precipitates become coarser, which contributes to the relatively low stress level. In addition, the strain rate sensitivity of the material is still significant, and the maximum elongation is greatly improved [30].

3.2. The Effect of Deformation Parameters on Maximum Elongation

The maximum elongation is an important indicator to quantify the plastic deformation capacity of materials. The influences of tensile temperature and strain rate on elongation can also be seen in Figure 3. With the increase in temperature, the maximum elongation of the studied alloy is enhanced. With the growth in strain rate, the maximum elongation is reduced. At 100 °C/0.1 s⁻¹, the elongation is only 0.19, while it increases to 0.50 at 400 °C/0.1 s⁻¹. Liu et al. [3] studied the hot tensile behavior of extruded 7075 alloy, and when tensile tested at 400 °C/0.1 s⁻¹, the maximum elongation was 0.40. Dynamic softening (such as dynamic recovery or dynamic recrystallization) is an important factor in determining maximum elongation. Higher temperatures and lower strain rates facilitate dynamic softening, which can enhance the maximum elongation. As the strain rate declines to 0.001 s⁻¹, the corresponding maximum elongation is 0.63. Generally, when deformed under high temperatures and low strain rates, the metal and alloy show excellent formability. In higher temperature conditions, the mobility of dislocation is enhanced, and the lower strain rate provides more deformation time for the dislocation movements.

3.3. The Effect of Deformation Parameters on the Flow Stress

The true stress with the corresponding strain 0.1 is selected to reveal the effect of strain rate on flow stress, which is displayed in Figure 3. At a constant tensile temperature, the flow stress increases with the increase in strain rate. With the growth in strain rate, the number of dislocations generated per unit of time increases, and the degree of dislocation motion is enhanced. Meanwhile, as plastic deformation time is shortened, the dynamic softening degree is weakened, so the flow stress increases. It can be seen from Figure 3 that under the condition of 100 °C, the strain rate sensitivity of the material is not obvious because the strengthening effect of the strain rate of the material is nearly equivalent to the softening effect of the material. However, at 200~400 °C, the material showed obvious positive strain rate sensitivity. This is because, under the condition of high-temperature deformation, the low strain rate leads to a significant softening and recovery effect of the alloy. At the same strain rate, the stress level of the material decreases with the increase in tensile deformation temperature. This is because with the increase in temperature, the resistance to dislocation movement decreases, and grain boundary slip is more likely to

occur. On the other hand, with the increase in temperature, the thermal motion of the atoms is intensified. The binding force between the atoms is weakened, and the recovery and recrystallization are more likely to occur at high temperatures, resulting in the enhancement of the metal softening effect.

3.4. The Constitutive Equation

The constitutive equation is an important aspect of investigating the thermal deformation behaviors of metal materials. It is capable of characterizing the relationship between flow stresses and processing parameters. Based on the constitutive equation and finite element method, the processing parameters of stamping, rolling, extruding, and so on can be optimized. Resultantly, experimentation costs can be dramatically reduced. According to the phenomenology, the Johnson–Cook material model was proposed and successfully employed in the finite element method for representing the stress and strain relationship of alloy materials [31]. The original Johnson–Cook model can be expressed as follows:

$$\sigma = (A + B\varepsilon^n)[1 + c \ln(\frac{\dot{\varepsilon}}{\dot{\varepsilon}_{ref}})][1 - (\frac{T - T_{ref}}{T_m - T_{ref}})^m] \quad (1)$$

where σ and ε are the equivalent stress and equivalent plastic strain, respectively; A represents the yield strength level at the reference deformation temperature and strain rate; B signifies the strain hardening factor; n is the strain hardening index; C is introduced to consider the strain rate sensitivity; $\dot{\varepsilon}$ and $\dot{\varepsilon}_{ref}$ denote the strain rate value and reference strain rate value; T indicates the deformation temperature; T_{ref} and T_m are the reference temperature and melting temperature of the experimental alloy; m is employed to consider the thermal softening effect at different deformation temperatures. In the present investigation, the reference strain rate is set at 0.001 s^{-1} , and $300 \text{ }^\circ\text{C}$ is selected as the reference temperature.

It can be observed that the first term of Equation (1) reveals the relationship between equivalent stress and equivalent plastic strain at the reference temperature and strain rate. The second and third terms exhibit the effect of strain rate and temperature on equivalent stress. Three terms in Equation (1) are mutually independent. In order to improve the accuracy and expand the applicability of the Johnson–Cook model, Lin et al. [32] proposed a modified Johnson–Cook model. It can be formulated as follows:

$$\sigma = (A_1 + B_1\varepsilon + B_2\varepsilon^2)(1 + C_1 \ln \dot{\varepsilon}^*) \exp[(\lambda_1 + \lambda_2 \ln \dot{\varepsilon}^*)T^*] \quad (2)$$

$$\dot{\varepsilon}^* = \frac{\dot{\varepsilon}}{\dot{\varepsilon}_{ref}} \quad (3)$$

$$T^* = T - T_{ref} \quad (4)$$

where A_1 , B_1 , B_2 , C_1 , λ_1 , and λ_2 denote the material parameters. It can be seen that the coupling effect of strain rate and temperature is considered in Equation (2). As a consequence, the accuracy of the Johnson–Cook model in characterizing the thermal flow behavior of metal materials is enhanced.

In order to obtain the parameters in Equation (2), a tensile test at a reference temperature ($300 \text{ }^\circ\text{C}$) with a strain rate of 0.001 s^{-1} was also conducted. The true stress–strain curve is depicted in Figure 4. It should be noted that at the reference deformation condition, Equation (2) can be simplified as:

$$\sigma = (A_1 + B_1\varepsilon + B_2\varepsilon^2) \quad (5)$$

A second-order polynomial fitting was performed on the yield deformation phase, and parameters of A_1 , B_1 , and B_2 , can be identified as 75.3, 36.9, and -69.1 , respectively. The comparison of the fitting curve and the measured curve is displayed in Figure 4 with the R-square value touching 0.983, manifesting that a good fitting precision was obtained.

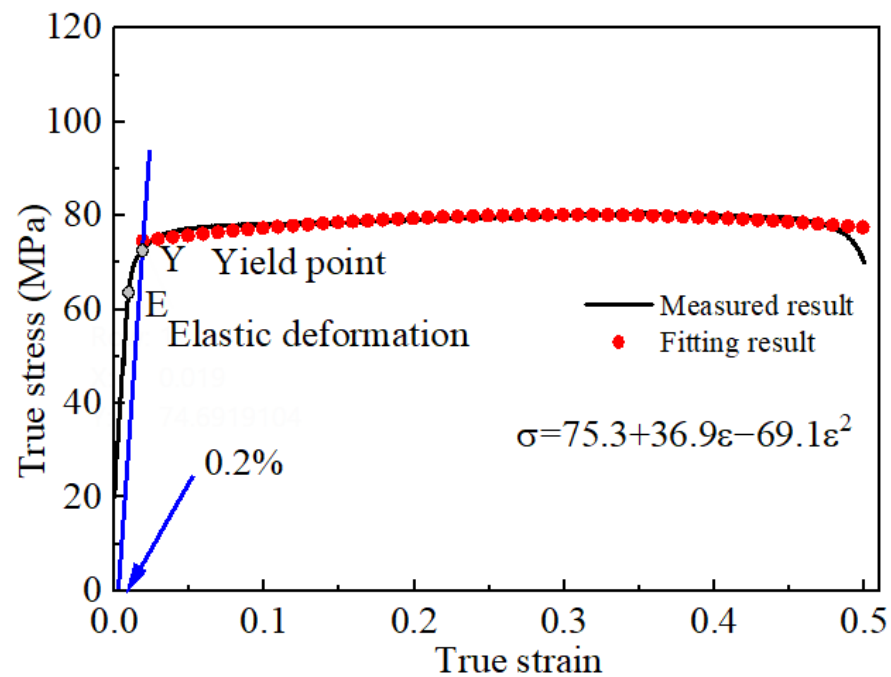


Figure 4. True stress strain curve of the as-cast 7005 alloy in tensile condition at the reference temperature and strain rate (300 °C, 0.001 s⁻¹).

At reference temperature (300 °C), the term $\exp[(\lambda_1 + \lambda_2 \ln \dot{\epsilon}^*)T^*]$ equals 1. Thus, Equation (2) can be rewritten as:

$$\sigma = (A_1 + B_1\epsilon + B_2\epsilon^2)(1 + C_1 \ln \dot{\epsilon}^*) \quad (6)$$

Based on Equation (6), the following expression can be obtained:

$$\frac{\sigma}{(A_1 + B_1\epsilon + B_2\epsilon^2)} = 1 + C_1 \ln \dot{\epsilon}^* \quad (7)$$

After plotting the relationship between $\sigma/(A_1 + B_1\epsilon + B_2\epsilon^2)$ and $\ln(\text{strain rate}^*)$, the slope of $\sigma/(A_1 + B_1\epsilon + B_2\epsilon^2) - \ln(\text{strain rate}^*)$ data at strain rates of 0.001, 0.01, and 0.1 can be recognized by linear fitting, which was 0.09. So, the parameter C_1 is 0.09. It can be seen in Figure 5.

In order to obtain λ_1, λ_2 , Equation (2) can be further transformed as:

$$\frac{\sigma}{(A_1 + B_1\epsilon + B_2\epsilon^2)(1 + C_1 \ln \dot{\epsilon}^*)} = \exp[(\lambda_1 + \lambda_2 \ln \dot{\epsilon}^*)T^*] \quad (8)$$

Taking the logarithm of Equation (8) on both sides, the following expression can be obtained:

$$\ln\left(\frac{\sigma}{(A_1 + B_1\epsilon + B_2\epsilon^2)(1 + C_1 \ln \dot{\epsilon}^*)}\right) = (\lambda_1 + \lambda_2 \ln \dot{\epsilon}^*)T^* \quad (9)$$

By plotting $\ln\{\sigma/[(A_1 + B_1\epsilon + B_2\epsilon^2)(1 + C_1 \ln(\text{strain rate}^*))]\}$ and T^* at different strain rate (0.001, 0.01, and 0.1 s⁻¹), the value of $\lambda = \lambda_1 + \lambda_2 \ln \dot{\epsilon}^*$ can be obtained. It is the slope of $\ln\{\sigma/[(A_1 + B_1\epsilon + B_2\epsilon^2)(1 + C_1 \ln(\text{strain rate}^*))]\} - T^*$. Through linear fitting, the slopes are identified as -0.0075, -0.00616, and -0.00496 at the strain rates of 0.001, 0.01, and 0.1 s⁻¹, respectively.

Further, the relationship between λ and $\ln(\text{strain rate}^*)$ can be plotted as depicted in Figure 6. By linear fitting, the λ_1 which is the intercept can be obtained. The value of λ_1 is

−0.00748, and the slope is 0.00055, which is the λ_2 value. Based on the above computation and analysis, the Johnson–Cook model can be expressed as:

$$\sigma = (75.3 + 36.9\varepsilon - 69.1\varepsilon^2)(1 + 0.09 \ln \dot{\varepsilon}^*) \exp[(-0.00748 + 0.00055 \ln \dot{\varepsilon}^*)T^*] \quad (10)$$

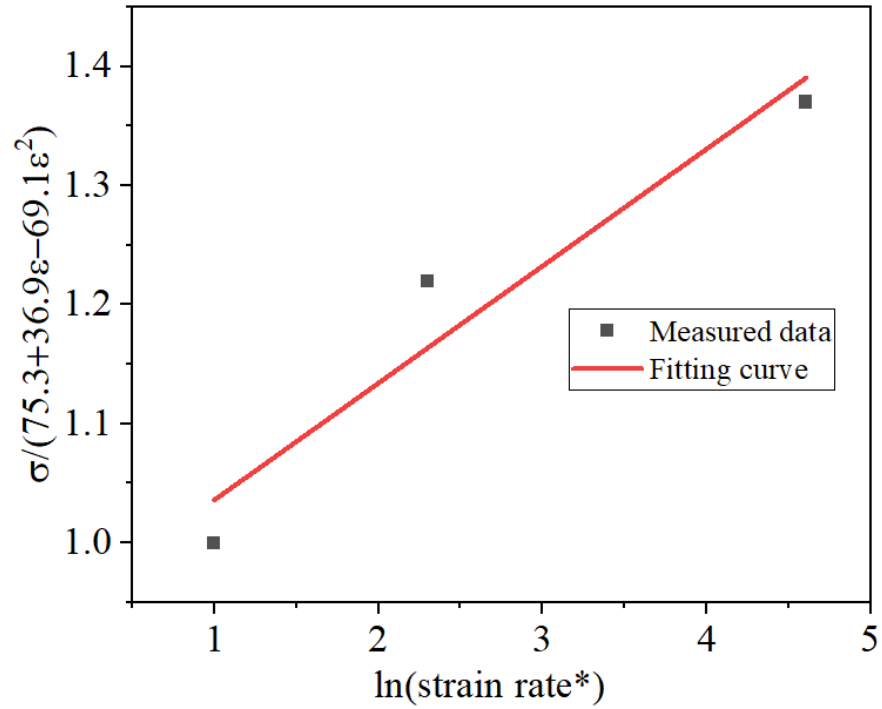


Figure 5. The relationship between $\sigma / (A_1 + B_1\varepsilon + B_2\varepsilon^2)$ and $\ln(\text{strain rate}^*)$.

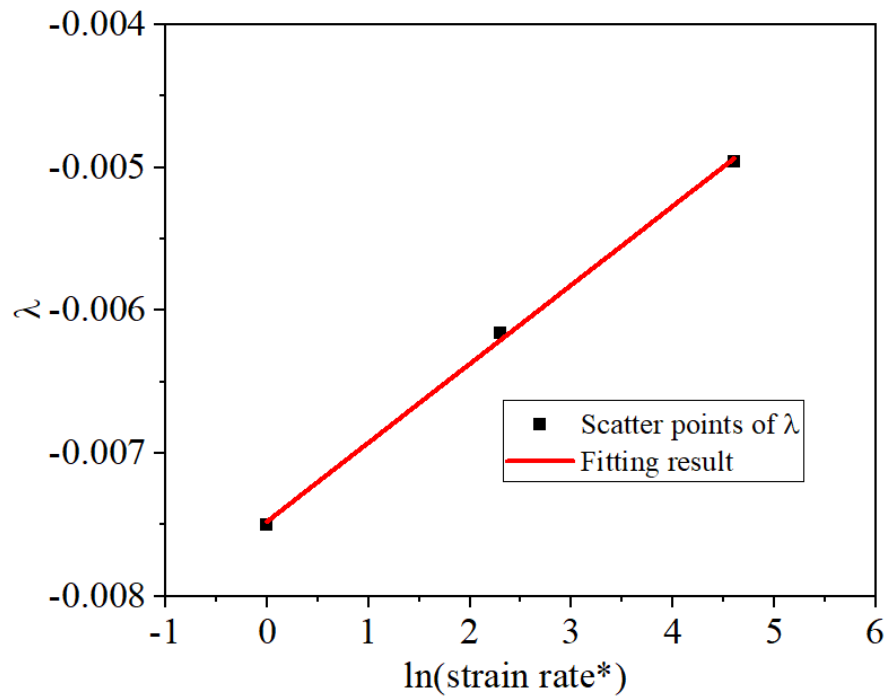


Figure 6. The relationship between λ and $\ln(\text{strain rate}^*)$.

In order to validate the accuracy of the Johnson–Cook model, the predicted and experimental true stress–strain curves were compared as shown in Figure 7. It can be

found that at 200 °C, 300 °C, and 400 °C, the consistency of predicted and experimental curves is acceptable. However, at a lower tensile temperature (100 °C), the accuracy of the Johnson–Cook model is unsatisfactory. This may derive from the fact that the stress is not very sensitive to the strain rate at low temperatures. These results are similar to those obtained by Lin et al. [32] and Wang et al. [31].

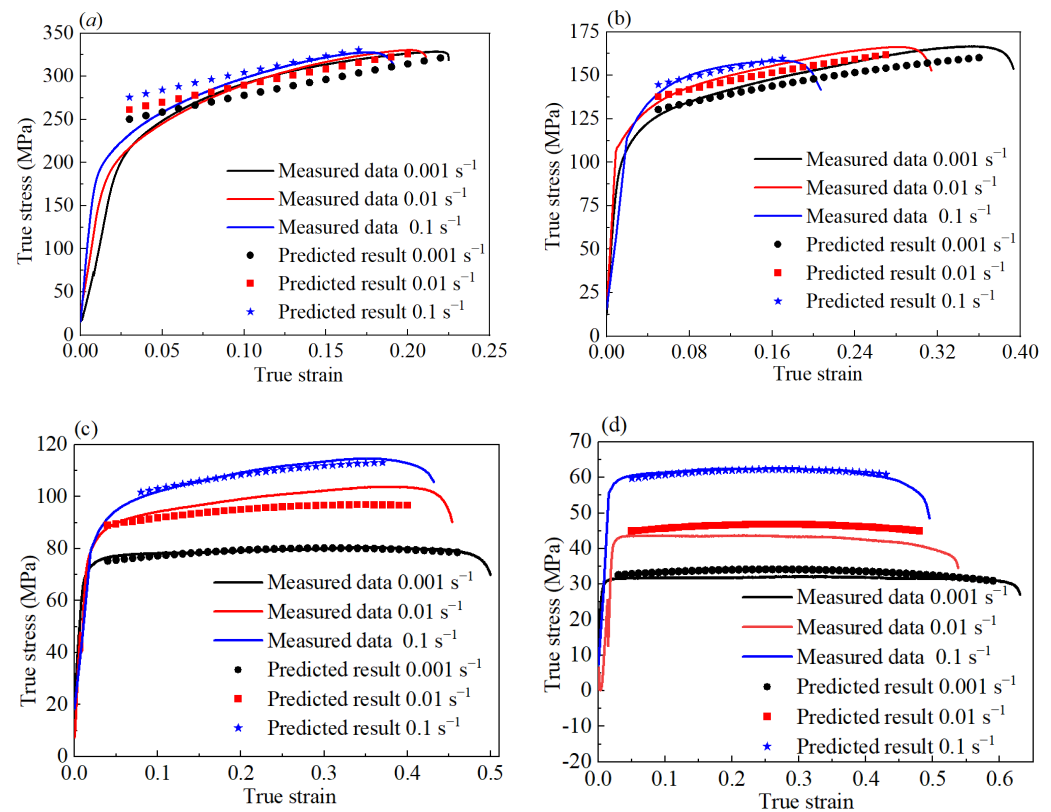


Figure 7. The comparison of predicted and measured true stress–strain curves at different deformation conditions: (a) 100 °C; (b) 200 °C; (c) 300 °C; (d) 400 °C.

3.5. SEM Observation

Figure 8 shows the effect of tensile temperature on the fracture morphology of the studied alloy with a constant strain rate. It can be observed from Figure 8a that under the deformation condition of 100 °C/0.001 s⁻¹, the dimples show a parabolic shape with a small size, and the distribution of dimples is uneven. In addition, some regions of the fracture surface exhibit a relatively flat fracture section, which is the obviously brittle fracture feature, indicating that the fracture mechanism at tensile condition 100 °C/0.001 s⁻¹ is a mixed fracture mechanism [33,34]. Shojaei et al. [2] explored the hot tensile properties of the 7075 aluminum alloy, and the results showed that when deformed at room temperature, intergranular fracture was the main failure mechanism. When stretched at elevated temperatures, void coalescence took place at the same time. When the temperature increases to 200 °C, as shown in Figure 8b, there are ductile characteristics in the shear fracture position. There are mainly small dimples, and a few larger and deeper dimples begin to appear. With further growth in tensile temperature, the brittle fracture characteristics of the tensile fracture disappear, and the fracture is dominated by microporous aggregation, with many rounded dimples. At the same time, the number of dimples increases, and the distribution is uniform. Some small dimples are distributed in some large equiaxial dimples, and the material shows ductile fracture features. With the increase in temperature, the dislocation is activated, which is conducive to dislocation slip, and thus the plastic deformation ability of the material is improved [35].

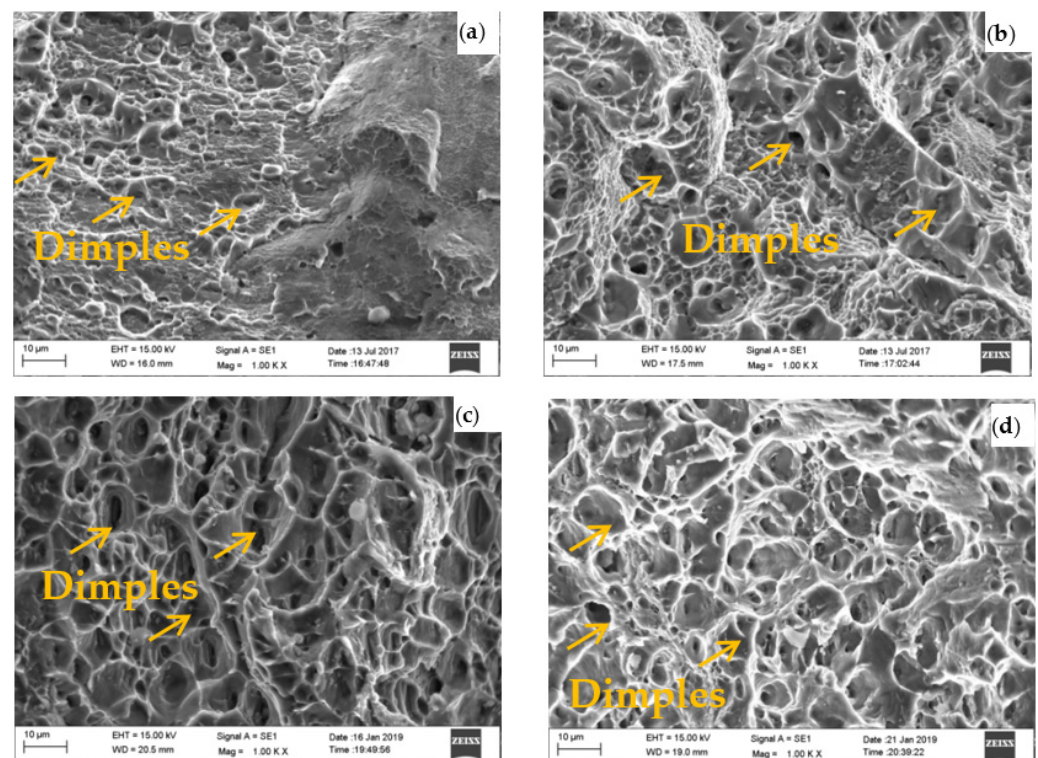


Figure 8. SEM observation of as-cast 7005 alloy fracture after hot tension at a strain rate of 0.001 s^{-1} . (a) $100 \text{ }^{\circ}\text{C}$; (b) $200 \text{ }^{\circ}\text{C}$; (c) $300 \text{ }^{\circ}\text{C}$; (d) $400 \text{ }^{\circ}\text{C}$.

3.6. OM Observation

Figure 9 shows the metallographic observation of the as-cast 7005 alloy after high-temperature tensile testing with a strain rate of 0.001 s^{-1} . The observation area is shown in Figure 2. It can be seen that the grain is elongated along the tensile direction under the tensile stress. Wang et al. [1] found that when the 7075 alloy deformed at $300 \text{ }^{\circ}\text{C}$, the grains were elongated along the tensile direction, and when stretched at $450 \text{ }^{\circ}\text{C}$, some equiaxed grains generated through recrystallization were observed. With the increase in temperature, the plastic deformation capacity of the alloy increases, so the grains become more slender. At high temperatures, the resistance of dislocation motion decreases. The grain boundary slip is more likely to generate, and recovery and recrystallization tend to occur at high temperatures, which enhances the softening effect [36]. As a consequence, the samples at high temperatures show more obvious plastic deformation ability. At the same time, with the increase in tensile deformation temperature, the number and size of holes near the fracture also increase. When the tensile temperature is $400 \text{ }^{\circ}\text{C}$, the holes in the material are more obvious.

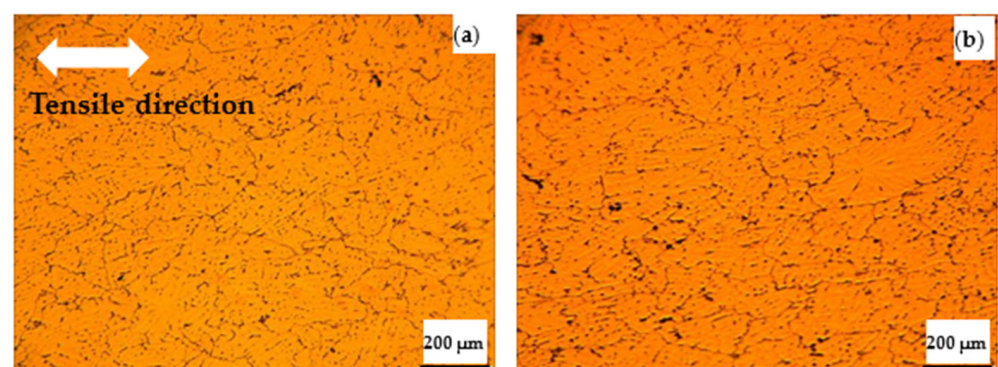


Figure 9. Cont.

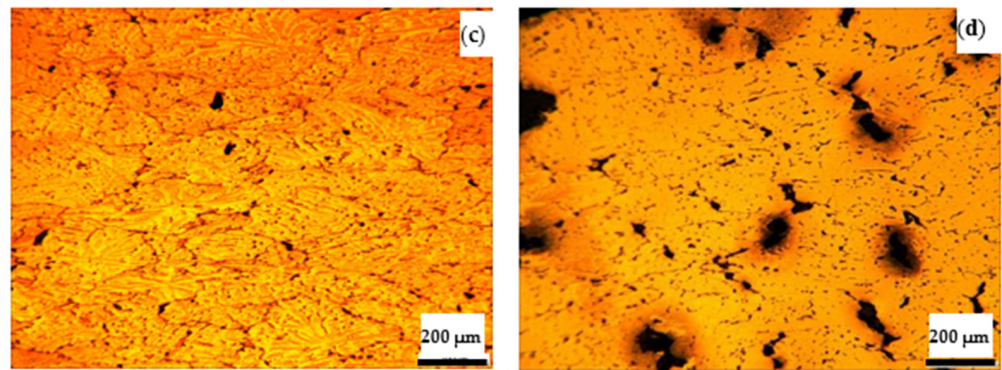


Figure 9. OM observation of the as-cast 7005 alloy near fracture after hot tension at 0.001 s^{-1} . (a) $100 \text{ }^{\circ}\text{C}$; (b) $200 \text{ }^{\circ}\text{C}$; (c) $300 \text{ }^{\circ}\text{C}$; (d) $400 \text{ }^{\circ}\text{C}$.

3.7. TEM Observation

Figure 10 shows the TEM graphs of the as-cast 7005 alloy after hot tensile tests with a strain rate of 0.001 s^{-1} . As can be seen from Figure 10a, after a tensile experiment at $100 \text{ }^{\circ}\text{C}$, a large number of high-density dislocation structures are generated in the material due to plastic deformation, and the pileup of dislocations is significant. With the increase in deformation temperature, as shown in Figure 10b,c, dislocation density is relatively reduced after tensile deformation at 200 and $300 \text{ }^{\circ}\text{C}$. This is because dislocation mobility is stronger under high-temperature conditions, and the phenomenon of dislocation disappearing is more significant [37,38]. At the same time, it was found that a small amount of fine precipitates appeared in the material. When the tensile temperature is $400 \text{ }^{\circ}\text{C}$, the dislocation density as shown in Figure 10d–f decreases significantly, and a large amount of precipitates are found. This indicates that the material has a dynamic precipitation process under the current deformation parameters [39]. With the decrease in strain rate, the number of precipitates increases. When deformed at a lower strain rate, there is enough time and energy for the dynamic precipitation process. It is widely acknowledged that precipitate plays a significant role in the deformation behavior of the aluminum alloy. During the process of plastic deformation, the interaction between fine precipitates and dislocations is mainly through the cutting mechanism. For coarse precipitates, the Orowan mechanism is dominant, and the shear stress of dislocations is relatively small. In addition, the coarsening precipitate is prone to becoming a crack source during the material stretching process, ultimately leading to a decrease in material strength and plasticity.

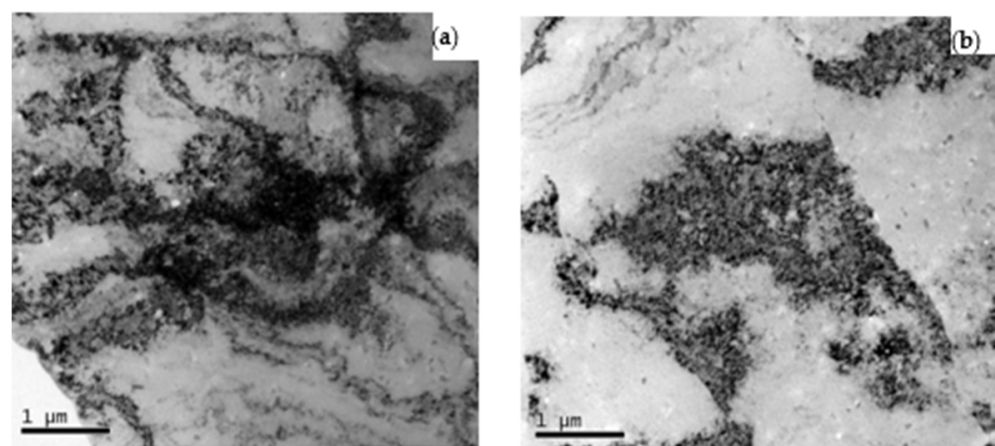


Figure 10. Cont.

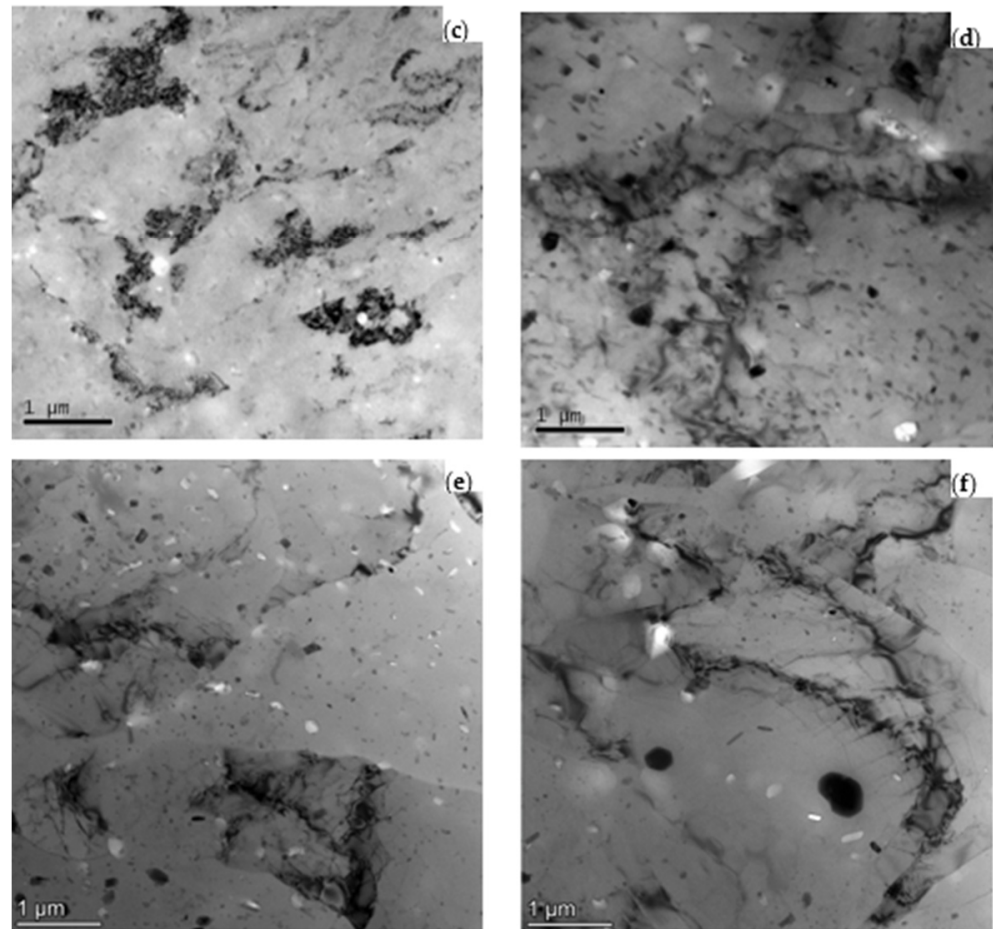


Figure 10. TEM observation of the as-cast 7005 alloy near fracture after hot tension in different conditions. (a) 100 °C 0.001 s⁻¹; (b) 200 °C 0.001 s⁻¹; (c) 300 °C 0.001 s⁻¹; (d) 400 °C 0.001 s⁻¹; (e) 400 °C 0.01 s⁻¹; (f) 400 °C 0.1 s⁻¹.

4. Conclusions

The hot tensile behavior, fracture features, and microstructure evolution of the as-cast 7005 aluminum alloy have been investigated under different tensile temperatures and strain rates. The following are the conclusions:

- (1) The flow stress of as-cast 7005 aluminum alloy decreases with the increase in tensile deformation temperature. In addition, the strain rate sensitivity of the material increases with increasing temperature. The Johnson–Cook model can be employed to characterize the thermal flow behavior of the targeted alloy.
- (2) The plastic deformation capacity of the as-cast 7005 aluminum alloy increases with the increase in temperature and the decrease in strain rate. Therefore, the grain at the fracture is continuously stretched with the increase in temperature, and the number and size of holes also increase. With the increase in tensile deformation temperature, the brittle fracture characteristics of the studied alloy disappear, and the fracture is dominated by microporous aggregation. The number and size of dimples increase, and the plastic deformation of the material is more significant.
- (3) In the process of tensile deformation, a large number of high-density dislocation structures are generated in the material due to plastic deformation. With the increase in tensile deformation temperature, the high-temperature conditions promote the elimination of dislocation, and the dislocation density decreases gradually. In addition, dynamic precipitation occurs inside the material.

Author Contributions: Conceptualization, T.Y.; Methodology, Y.W. and L.L.; Data curation, E.X. and H.Y.; Formal analysis, T.Y., H.Y. and J.T.; Funding acquisition, Y.W.; Investigation, T.Y.; Resources, E.X. and W.L.; Writing—original draft, E.X. and T.Y.; Validation, J.T. and W.L.; Visualization, E.X. and L.L.; Supervision, Y.W.; Writing—review and editing, E.X., H.Y. and Y.W. All authors have read and agreed to the published version of the manuscript.

Funding: The research described in this paper was supported by the National Natural Science Foundation of China (52201074, 52171115), the Scientific Research Fund of the Hunan Provincial Education Department of China (22A0626, 23A0633), the College Student Innovation and Entrepreneurship Project (S202311528045, S202311528117), and the Aid Program for Science and Technology Innovative Research Team in Higher Educational Institutions of Hunan Province.

Data Availability Statement: Data is contained within the article.

Conflicts of Interest: The authors declare no conflicts of interest.

References

- Omiyale, B.O.; Olugbade, T.O.; Abioye, T.E.; Farayibi, P.K. Wire arc additive manufacturing of aluminium alloys for aerospace and automotive applications: A review. *Mater. Sci. Technol.* **2022**, *38*, 391–408. [[CrossRef](#)]
- Wu, B.; Pan, Z.; Ding, D.; Cuiuri, D.; Li, H.; Xu, J.; Norrish, J. A review of the wire arc additive manufacturing of metals: Properties, defects and quality improvement. *J. Manuf. Process.* **2018**, *35*, 127–139. [[CrossRef](#)]
- Zang, Q.; Chen, H.; Lee, Y.-S.; Yu, H.; Kim, M.-S.; Kim, H.-W. Improvement of anisotropic tensile properties of Al-7.9Zn-2.7Mg-2.0Cu alloy sheets by particle stimulated nucleation. *J. Alloys Compd.* **2020**, *828*, 154330. [[CrossRef](#)]
- Lewis, G.M.; Buchanan, C.A.; Jhaveri, K.D.; Sullivan, J.L.; Kelly, J.C.; Das, S.; Taub, A.I.; Keoleian, G.A. Green Principles for Vehicle Lightweighting. *Environ. Sci. Technol.* **2019**, *53*, 4063–4077. [[CrossRef](#)] [[PubMed](#)]
- Xu, L.; Xin, Y.; Ma, L.; Zhang, H.; Lin, Z.; Li, X. Challenges and solutions of cathodic protection for marine ships. *Corros. Commun.* **2021**, *2*, 33–40. [[CrossRef](#)]
- Tiwary, A.; Kumar, R.; Chohan, J.S. A review on characteristics of composite and advanced materials used for aerospace applications. *Mater. Today Proc.* **2021**, *51*, 865–870. [[CrossRef](#)]
- Zhou, B.; Liu, B.; Zhang, S.; Lin, R.; Jiang, Y.; Lan, X. Microstructure evolution of recycled 7075 aluminum alloy and its mechanical and corrosion properties. *J. Alloys Compd.* **2021**, *879*, 160407. [[CrossRef](#)]
- Ma, Z.; Ji, H.; Huang, X.; Xiao, W.; Tang, X. Research on High Temperature Stamping Forming Performance and Process Parameters Optimization of 7075 Aluminum Alloy. *Materials* **2021**, *14*, 5485. [[CrossRef](#)]
- Wang, L.; Tao, S.; Zhu, P.; Chen, W. Data-driven topology optimization with multiclass microstructures using latent variable Gaussian process. *J. Mech. Des.* **2021**, *143*, 031708. [[CrossRef](#)]
- Zhang, W.; Xu, J. Advanced lightweight materials for Automobiles: A review. *Mater. Des.* **2022**, *221*, 110994. [[CrossRef](#)]
- Edwards, D.M.; Rawat, D.B. Quantum Adversarial Machine Learning: Status, Challenges and Perspectives. In Proceedings of the 2020 Second IEEE International Conference on Trust, Privacy and Security in Intelligent Systems and Applications (TPS-ISA), Atlanta, GA, USA, 28–31 October 2020.
- Tang, J.; Liu, M.; Bo, G.; Jiang, F.; Luo, C.; Teng, J.; Fu, D.; Zhang, H. Unraveling precipitation evolution and strengthening function of the Al-Zn-Mg-Cu alloys with various Zn contents: Multiple experiments and integrated internal-state-variable modeling. *J. Mater. Sci. Technol.* **2022**, *116*, 130–150. [[CrossRef](#)]
- Tang, J.; Wang, J.; Teng, J.; Wang, G.; Fu, D.; Zhang, H.; Jiang, F. Effect of Zn content on the dynamic softening of Al-Zn-Mg-Cu alloys during hot compression deformation. *Vacuum* **2021**, *184*, 109941. [[CrossRef](#)]
- Guo, Y.; Zhang, J.; Zhao, H. Microstructure evolution and mechanical responses of Al-Zn-Mg-Cu alloys during hot deformation process. *J. Mater. Sci.* **2021**, *56*, 13429–13478. [[CrossRef](#)]
- Wang, H.; Wang, C.; Mo, Y.; Wang, H.; Xu, J. Hot deformation and processing maps of Al-Zn-Mg-Cu alloy under coupling-stirring casting. *J. Mater. Res. Technol.* **2019**, *8*, 1224–1234. [[CrossRef](#)]
- Wang, Z.; Zhang, Z.; Lang, Q.; Song, G.; Liu, L. Microstructure evolution and deformation behavior of TIG welded 7075-T6 aluminum alloy followed by partial hot rolling. *J. Manuf. Process.* **2023**, *94*, 524–538. [[CrossRef](#)]
- Tian, N.; Jiang, X.; Zhang, Y.; Zeng, Z.; Wang, T.; Zhao, G.; Qin, G. Effect of Precipitates on the Mechanical Performance of 7005 Aluminum Alloy Plates. *Materials* **2022**, *15*, 5951. [[CrossRef](#)] [[PubMed](#)]
- Hou, J.; Deng, P.; Wang, S.; Xu, H.; Shi, Y. Study on formability and microstructure evolution of hot deep drawing manufactured 7005 aluminum alloy sheet metal. *Mater. Today Commun.* **2023**, *36*, 106794. [[CrossRef](#)]
- Chaskis, S.; Stachouli, E.; Gavalas, E.; Bouzouni, M.; Papaefthymiou, S. Microstructure, phase formation and heat-treating of novel cast Al-Mg-Zn-Cu-Si lightweight complex concentrated aluminum based alloy. *Materials* **2022**, *15*, 3169. [[CrossRef](#)]
- Kulkarni, S.M. Effect of geometric irregularities induced during manufacturing of a crash-box on its crashworthiness performance. *Mater. Today Proc.* **2022**, *57*, 715–721. [[CrossRef](#)]
- Chen, L.; Zhao, G.; Yu, J.; Zhang, W. Constitutive analysis of homogenized 7005 aluminum alloy at evaluated temperature for extrusion process. *Mater. Des.* **2015**, *66*, 129–136. [[CrossRef](#)]

22. Duan, Y.; Tang, L.; Xu, G.; Deng, Y.; Yin, Z. Microstructure and mechanical properties of 7005 aluminum alloy processed by room temperature ECAP and subsequent annealing. *J. Alloys Compd.* **2016**, *664*, 518–529. [[CrossRef](#)]
23. Jiang, J.; Atkinson, H.; Wang, Y. Microstructure and mechanical properties of 7005 aluminum alloy components formed by thixoforming. *J. Mater. Sci. Technol.* **2017**, *33*, 10. [[CrossRef](#)]
24. Liu, M.; Shan, Z.; Li, X.; Zang, Y. Hot tensile deformation behavior and microstructure evolution of 7075 aluminum alloy sheet. *J. Mater. Res. Technol.* **2023**, *24*, 724–736. [[CrossRef](#)]
25. Fu, R.; Liang, Y.; Han, Q.; Guo, Y.; Lei, H.; Liu, C. Strengthening and fracturing mechanisms of laser-directed energy deposited Al-7075 alloy. *Mater. Sci. Eng. A* **2023**, *881*, 145433. [[CrossRef](#)]
26. Xiao, W.; Wang, B.; Wu, Y.; Yang, X. Constitutive modeling of flow behavior and microstructure evolution of AA7075 in hot tensile deformation. *Mater. Sci. Eng. A* **2018**, *712*, 704–713. [[CrossRef](#)]
27. Zang, Q.; Yu, H.; Lee, Y.-S.; Kim, M.-S.; Kim, H.-W. Hot deformation behavior and microstructure evolution of annealed Al-7.9Zn-2.7Mg-2.0Cu (wt%) alloy. *J. Alloys Compd.* **2018**, *763*, 25–33. [[CrossRef](#)]
28. Wu, H.; Wen, S.; Huang, H.; Gao, K.; Wu, X.; Wang, W.; Nie, Z. Hot deformation behavior and processing map of a new type Al-Zn-Mg-Er-Zr alloy. *J. Alloys Compd.* **2016**, *685*, 869–880. [[CrossRef](#)]
29. Zhao, J.; Deng, Y.; Tan, J.; Zhang, J. Effect of strain rate on the recrystallization mechanism during isothermal compression in 7050 aluminum alloy. *Mater. Sci. Eng. A* **2018**, *734*, 120–128. [[CrossRef](#)]
30. Zheng, J.-H.; Pruncu, C.; Zhang, K.; Zheng, K.; Jiang, J. Quantifying geometrically necessary dislocation density during hot deformation in AA6082 Al alloy. *Mater. Sci. Eng. A* **2021**, *814*, 141158. [[CrossRef](#)]
31. Wang, Y.; Xing, J.; Zhou, Y.; Kong, C.; Yu, H. Tensile properties and a modified s-Johnson-Cook model for constitutive relationship of AA7075 sheets at cryogenic temperatures. *J. Alloys Compd.* **2023**, *942*, 169044. [[CrossRef](#)]
32. Lin, Y.C.; Chen, X.M.; Liu, G. A modified Johnson–Cook model for tensile behaviors of typical high-strength alloy steel. *Mater. Sci. Eng. A* **2010**, *527*, 6980–6986. [[CrossRef](#)]
33. Taheri-Mandarjani, M.; Zarei-Hanzaki, A.; Abedi, H.R. Hot ductility behavior of an extruded 7075 aluminum alloy. *Mater. Sci. Eng. A* **2015**, *637*, 107–122. [[CrossRef](#)]
34. Jiang, J.-F.; Wang, Y.; Liu, Y.-Z.; Xiao, G.-F.; Li, H. Microstructure and mechanical properties of 7005 aluminum alloy processed by one-pass equal channel reciprocating extrusion. *Trans. Nonferrous Met. Soc. China* **2021**, *31*, 609–625. [[CrossRef](#)]
35. Mao, W.-M.; Zhu, W.-Z. Tensile properties and microstructure of rheo-diecast 7075 alloy prepared by serpentine channel process. *China Foundry* **2019**, *16*, 161–167. [[CrossRef](#)]
36. Li, G.; Ding, H.; Wang, J.; Zhang, N.; Hou, H. Superplastic tensile deformation behavior and microstructural evolution of Al–Zn–Mg–Cu alloy. *Metals* **2019**, *9*, 941. [[CrossRef](#)]
37. Lu, J.; Song, Y.; Zhou, P.; Lin, J. Rheological behavior and dynamic softening mechanism of AA7075 sheet under isothermal tensile deformation. *J. Mater. Res. Technol.* **2020**, *9*, 9784–9797. [[CrossRef](#)]
38. Ye, T.; Wu, Y.; Liu, A.; Xu, C.; Li, L. Mechanical property and microstructure evolution of aged 6063 aluminum alloy under high strain rate deformation. *Vacuum* **2019**, *159*, 37–44. [[CrossRef](#)]
39. Wang, L.; Yu, H.; Lee, Y.-S.; Kim, M.-S.; Kim, H.-W. Effect of microstructure on hot tensile deformation behavior of 7075 alloy sheet fabricated by twin roll casting. *Mater. Sci. Eng. A* **2016**, *652*, 221–230. [[CrossRef](#)]

Disclaimer/Publisher’s Note: The statements, opinions and data contained in all publications are solely those of the individual author(s) and contributor(s) and not of MDPI and/or the editor(s). MDPI and/or the editor(s) disclaim responsibility for any injury to people or property resulting from any ideas, methods, instructions or products referred to in the content.